Crystallographic Disorder and Strong Magnetic Anisotropy in Dy₃Pt₂Sb_{4.48}

Terry Paske, ^a Yingdong Guan, ^b Chaoguo Wang, ^a Curtis Moore, ^c Zhiqiang Mao, ^b Xin Gui ^{a*}

Abstract

We report the crystal growth and characterization of a rare-earth-containing material, $Dy_{3.00(1)}Pt_2Sb_{4.48(2)}$. This compound possesses a similar structure to the previously reported $Y_3Pt_4Ge_6$, but lacks two layers of Pt atoms. Crystallographic disorder was found in $Dy_{3.00(1)}Pt_2Sb_{4.48(2)}$. Additionally, the Dy-Dy framework was found to have both square net and triangular lattices. $Dy_{3.00(1)}Pt_2Sb_{4.48(2)8}$ was determined to be antiferromagnetically ordered around ~15 K while a competing antiferromagnetic sublattice also exists at lower temperature. Strong magnetic anisotropy was observed and several metamagnetic transitions were seen in the hysteresis loops. Furthermore, the Curie-Weiss fitting revealed unusually small effective moment of Dy, which is far below the expected value of Dy^{3+} (10.65 μ_B). This material might provide a new platform to study the relation between crystallographic disorder and magnetism.

^a Department of Chemistry, University of Pittsburgh, Pittsburgh, PA, 15260, USA

^b Department of Physics, Pennsylvania State University, University Park, PA, 16801, USA

^c Department of Chemistry and Biochemistry, The Ohio State University, Columbus, OH, 43210, USA

Introduction

Rare-earth-based materials are of great importance for the investigation of frustrated magnets since they possess highly localized moments and their ability to crystallize into various structural types. It is well known that magnetic frustration commonly results from the competing antiferromagnetic (AFM) interactions between the nearest neighbors or even the next nearest neighbors. ^{1,2} To allow such competition, geometric frustration of the sublattice of magnetic atoms is one of the most important routes to realizing frustrated magnetism. The most widely investigated frustrated structural motifs (YbMgGaO₄),³⁻⁶ Kagome lattice (ZnCu₃(OH)₆Cl₂)^{3,7-9} include triangular lattice pyrochlore/breathing pyrochlore lattice (Ce₂Sn₂O₇/Ba₃Yb₂Zn₅O₁₁). ^{10–14} These structural motifs are all composed of triangles. Ideally, equilateral triangles should exist in such systems and their frustration can be "isotropic". However, square lattices were also found to be great motifs for magnetic frustration since it can be seen as two edge-shared isosceles right triangles. 15-17 Thus when the competing exchange coupling between the nearest neighbors (J_1) and the next nearest neighbors (J_2) fall into an appropriate region, magnetic frustration can be expected. 18

Y₃Pt₄Ge₆ was reported to crystallize in the *P* 2₁/*m* space group.¹⁹ In recent years, the crystal structure and magnetic properties of polycrystalline Ln₃Pt₄Ge₆ (Ln = Y, Ce, Pr, Nd, Sm, Gd-Dy) were reinvestigated^{20,21} and isostructural Yb₃Pt₄Si_{6-x}²² was also discovered. What is interesting about Ln₃Pt₄Ge₆ is that the atoms on the Ln site construct frameworks of both tilted square lattice and triangular lattice. The magnetic properties measurements of these materials revealed that only Gd₃Pt₄Ge₆ and Tb₃Pt₄Ge₆ were antiferromagnetically ordered while others were paramagnetic.²⁰ Pure phase of polycrystalline Dy₃Pt₄Ge₆ could not be synthesized and thus its magnetic properties were not reported.²⁰

Here, we replaced Ge with Sb and obtained mm-sized single crystals of Dy_{3.00(1)}Pt₂Sb_{4.48(2)} with crystallographic disorder on both Dy and Sb sites. Dy_{3.00(1)}Pt₂Sb_{4.48(2)} appears to be a new material which crystallizes in a similar structure type as RE₃Pt₄Ge₆. By performing magnetic properties and electrical transport measurements, we observed complex magnetic behavior in Dy_{3.00(1)}Pt₂Sb_{4.48(2)} including strong magnetic anisotropy, competing AFM sublattices and multiple metamagnetic transitions. We believe that Dy_{3.00(1)}Pt₂Sb_{4.48(2)} will provide a platform for investigating the relation between crystallographic disorder and magnetism as well as frustrated magnetism.

Experimental Details

Single Crystal Growth: The self-flux method with excess Sb was employed to obtain single crystals of Dy_{3.00(1)}Pt₂Sb_{4.48(2)}. Dy powder (99.9%, ~400 mesh, Alfa Aesar), Pt powder (>99.9%, ~325 mesh, Thermo Scientific) and Sb powder (99.5%, ~100 mesh, Thermo Scientific) in the molar ratio of 3:2:50 were mixed in an alumina crucible in an Ar-filled glovebox. This crucible was put into an quartz tube, with quartz wool and some glass pieces above to assist the separation of the Sb flux from the crystals after cooling. The tube was purged with argon and then evacuated (<5×10⁻³ Torr) and sealed. It was heated in a box furnace to 900 °C and held for 12 hours followed directly by another heat treatment at 1100 °C for two days. After one day of heating at 1100 °C, the tube was gently agitated, during which, the temperature within did not drop below 1000 °C. The furnace was slowly cooled at the rate of 1 °C per hour to 750 °C, where it remained for a few hours then the Sb flux was centrifuged out. Water quenching the tube afterwards solidified the Sb flux in the wool plug for simple separation from the crystals. Striped crystals with dimensions up to 0.1 x 0.25 x 3 mm³ were obtained, as shown in Figure 1(a). The crystals are stable in air.

Structure and Phase Determination: The single crystal X-ray diffraction studies were carried out on a Bruker Kappa Photon III CPAD diffractometer equipped with Mo K_{α} radiation (λ = 0.71073 Å). A 0.125 x 0.093 x 0.043 mm piece of a metallic silver block was mounted on a MiTeGen Micromount with Paratone 24EX oil. Data were collected in a nitrogen gas stream at 125(2) K using ϕ and ϖ scans. Crystal-to-detector distance was 50 mm using variable exposure time (2-5 s) depending on θ with a scan width of 1.0°. Bruker SMART software with corrections for Lorentz and polarization effects included was utilized for data requisition. Numerical absorption correction was applied based on crystal-face-indexing using *XPREP*. The direct method and full-matrix least-squares on F^2 procedure within the SHELXTL package were employed to solve the crystal structure. Powder X-ray diffraction patterns on crushed crystals, obtained with a Bruker D2 Phaser diffractometer with Cu K α radiation and a LYNXEYE-XE detector, were consistent with the structure determined by single crystal diffraction.

Scanning Electron Microscopy (SEM)-Energy-Dispersive X-ray Spectroscopy (EDS): The high vacuum SEM (ThermoFisher Apreo HiVac with EDAX Elite 150 SDD EDS detector) was used to determine the chemical composition. Samples were mounted on carbon tape before loading into the

SEM chamber. Multiple points and areas were examined from each sample to get the Dy: Pt: Sb ratio. Samples were analyzed at 20 kV, and the spectra were collected for 100 seconds to get the chemical composition via APEX EDS software.

Physical Property Measurement: Oriented single crystal samples were utilized for physical properties measurement. The magnetic properties were measured on a Quantum Design SQUID magnetometer from 2-300 K under the external magnetic field of 0-7 T. The electrical transport measurement was conducted on a Quantum Design PPMS from 2.5 K to 300 K under the external magnetic field of 0-9 T using a four-probe method.

Electronic Structure Calculations: Calculations of Crystal Orbital Hamiltonian Population (COHP) was performed by Tight-Binding, Linear Muffin-Tin Orbital-Atomic Spheres Approximation (TB-LMTO-ASA) using the Stuttgart code.^{25–27} A mesh of 1000 *k* points was used to generate all integrated values.²⁸ The number of irreducible k-points is 70. Energy difference of 0.05 meV was set as the convergence criterion. In the ASA method, space was filled with overlapping Wigner-Seitz (WS) spheres. The symmetry of the potential was treated as spherical in each WS sphere with a combined correction on the overlapping part. The WS radii were: 3.67 Å for Dy; 2.59 Å for Pt; and 3.30 Å for Sb. Empty spheres were required for the calculation, and the overlap of WS spheres was limited to no more than 16%.

Band structure and density of states (DOS) were calculated by using WIEN2k, which employs the full-potential linearized augmented plane wave method (FP-LAPW) with local orbitals implemented. The electron exchange-correlation potential used was the generalized gradient approximation. The conjugate gradient algorithm was applied. Reciprocal space integrations were completed over a $5\times10\times3$ Monkhorst-Pack k-point mesh. Orbital potentials (U = 4 eV) were employed for Dy f electrons. With these settings, the calculated total energy converged to less than 0.1 meV per atom.

Results and Discussion

Crystal Structure Determination: By performing single-crystal X-ray diffraction, the formula of the striped crystals was determined to be Dy_{3.00(1)}Pt₂Sb_{4.48(2)}, which crystallizes in the monoclinic space group $P 2_1/m$ (No. 11, mP19) and is found to be a new material in the Dy-Pt-Sb ternary system. The crystallographic data, including atomic positions, site occupancies, and refined anisotropic displacement parameters (and equivalent isotropic thermal displacement parameters) are listed in Tables 1, 2 and 3. In our crystallographic model, the best solution emerged when multiple disordered sites were introduced, as shown in Figure 1(b) where 12 disordered sites can be found and six of them (Dy1, Sb1, Sb1' and Dy2, Sb2, Sb2') are symmetrically equivalent with the rest correlated by the 2₁ symmetry. Here we correlate Dy1 with Sb1 and Sb1' as well as Dy2 with Sb2 and Sb2', indicating that Dy1(2) site exists only when Sb1(1) and Sb1'(2') appear. The interatomic distances between Dy1/Dy2 and Sb2 (Sb2')/Sb1 (Sb1') are ~1.29 Å. These are not possible bond lengths as they are far below 50% of the common Dy-Sb bond lengths, for example, 3.0660 (2) Å in DySb^{33,34}. Moreover, by removing either set of Dy and Sb atoms, a large residual peak and hole can appear, as can be seen in Table S1. Therefore, in order to obtain reasonable crystallographic refinement results, two constraints must be applied to the crystallographic model: 1. The sum of the occupancies of Dy1 and Dy2 was set to be 100%; 2. The occupancies of sites Sb1, Sb1', Sb2 and Sb2' were set to be correlated and relaxed. In such condition, Sb1 and Sb1' turned to possess higher occupancies (~20% for each site) than Sb2 and Sb2' (~4% for each site) and the interatomic distances between Dy1-Sb1 (3.023 (3) Å), and Dy2-Sb2 (3.02 (2) Å) pairs are comparable with literature about compounds in Dy-Sb binary system and elemental Sb. 33-34 The bond length of Sb1-Sb1' (2.579 (4) Å) and Sb2-Sb2' (2.60 (3) Å) are smaller than literature³⁵. Considering that such Sb pairs exist as split interstitial, which can usually lead to short bond length, the short Sb-Sb bond length in this work is reasonable. Under such constraints, the crystallographic disorder with very short Dy-Sb distances can thus be interpreted in a reasonable way that the Dy1, Sb1 and Sb1' sites are occupied alternately with the Dy2, Sb2 and Sb2' sites based on the site occupancies shown in Table 2. A comparison of crystallographic refinement results with different models has also been summarized in Table S1. The inclusion of Sb2(Sb2') and Dy2 significantly improves the results. As shown in Figure 1(c), sites Dy1 and the Sb1 and Sb1' pair make up setting #1, and Dy2 and the Sb2 and Sb2' pair make up setting #2. Same coordination environment of Dy can be found in both settings. Two types of Dy@Sb₈ polyhedra are shown on the left of Figure 1(d). Additionally, when coordinated with Pt atoms, the partially-occupied Dy forms Dy@Pt₆ trigonal prisms while fully-occupied Dy constructs Dy@Pt₂ zig-zag chain. When bonded together, the fully-occupied Dy atoms exhibits a distorted square net framework, as shown in Figure 1(e). Moreover, partially-occupied Dy1 atoms construct a puckered triangular lattice. The Dy framework can be seen as extending two-dimensionally within the *ab* plane and stacking along the *c* axis.

To confirm the chemical composition, the SEM-EDS measurements were performed on two different crystals from different batches. The EDS results averaged from five points are shown in Table S2 in the Supplementary Information. The average formula was determined to be Dy_{3.1(3)}Pt_{2.0(7)}Sb_{3.8(4)} when normalized to the concentration of Pt, which is consistent with the results from the single-crystal X-ray diffraction measurement. Moreover, powder X-ray diffraction pattern of the crystals is illustrated in Figure S1, which implies high purity of the crystals. A preferred orientation of (001) is clearly seen in the powder XRD pattern.

Structural Relations and Bonding Analysis: When considering several repeats of the unit cell along the *c* axis, certain structural motifs within previously reported structures can be identified. Both YIrGe₂ and YbSb₂ have a top and bottom motif that are symmetrical about a mirror plane through the center of the unit cell horizontally, Figure 2(a) (Left) and (Right) respectively. The setting#1 of Dy_{3.00(1)}Pt₂Sb_{4.48(2)} can be seen as the intergrowth of alternating slabs of YIrGe₂ and YbSb₂ along the *c* axis, shown in Figure 2(a) (Middle). The adjacent YIrGe₂ and YbSb₂ slabs share a layer of Dy and Sb in Dy_{3.00(1)}Pt₂Sb_{4.48(2)}. As for the setting#2 of Dy_{3.00(1)}Pt₂Sb_{4.48(2)}, the order of the top and bottom halves of YIrGe₂ switch, which is not shown here. This repeating motif in Dy_{3.00(1)}Pt₂Sb_{4.48(2)} is similar to repeat slabs in Y₃Pt₄Ge₆ for which previous reports¹⁹ claimed to be built from alternating YIrGe₂-type and ThCr₂Si₂-type^{36,37} slabs. However, as can be seen in Figure 2(b), the alternating layer in Y₃Pt₄Ge₆ contains two layers of Pt atoms which are missing in Dy_{3.00(1)}Pt₂Sb_{4.48(2)}.

To better understand how the crystallographic disordering affects the structure of Dy_{3.00(1)}Pt₂Sb_{4.48(2)}, COHP calculations were performed for both settings. The relevant chemical bonds for disordered Dy1 and Dy2 are visualized in Figure 3(b) & 3(c) respectively. All bond lengths were set to be no longer than 3.5 Å. Figure 3(a) presents the COHP curves for both settings where the positive part of the x axis indicates bonding interaction, and the negative part shows anti-bonding

interaction. Similar behaviors can be found for Dy1(Dy2)-Sb1(Sb2) and Dy1(Dy2)-Sb1'(Sb2') as well as Dy1(Dy2)-Pt1 and Dy1(Dy2)-Pt2. The disordered Dy in both settings shows nearly all anti-bonding features when bonded with the surrounding atoms within the visible energy range (-4 eV to 2 eV). Such behavior indicates that the disordered Dy1 and Dy2 sites both destabilize the structure from -4 eV to 2 eV, which might explain why they are both partially occupied. More COHP curves for Dy-Pt, Dy-Sb, Pt-Sb and Sb-Sb bonds can be found Figure S2 in the Supporting Information, which demonstrates significant anti-bonding interaction above ~ -2.5 eV.

Magnetic Characterization: Magnetic property measurements were performed on Dy_{3.00(1)}Pt₂Sb_{4.48(2)} single crystals with the magnetic field applied along two directions, perpendicular to the *ab* plane ($H\perp ab$), and parallel to the *a* axis (H//a). The orientation of a representative stripe-like crystal is shown in the inset of Figure 4(a). The temperature-dependence of magnetic susceptibility (χ) and inverse χ under an applied magnetic field of 1000 Oe from 2 to 300 K are shown in Figure 4(a) and 4(c). Both curves were collected under field-cooling (FC) history. We observed distinct magnetic anisotropy from the data presented in Figure 4(a-b). When the field (H) is perpendicular to the *ab* plane (Figure 4(a)), an AFM transition can be found around $T_{N1} \sim 17$ K while another peak is seen at $T_{N2} \sim 4.5$ K. The magenta curve in Figure 4(a) shows the temperature dependence of $1/\chi$. When the external magnetic field is parallel to the *a* axis, the χ vs T curve exhibits different behavior. As shown in the main panel of Figure 4(c), the magnetic susceptibility increases with decreasing temperature until a kink is seen at ~ 15.9 K, indicating the spin easy axis is within the ab-plane. Upon further cooling, another sharp peak appears at ~ 3.9 K. We fitted the $1/\chi$ data using the modified Curie-Weiss (CW) law,

$$\chi = \chi_0 + \frac{c}{T - \theta_{CW}} ,$$

where χ is the magnetic susceptibility of the material, χ_0 and C are independent of temperature (the latter related to the effective moment and the former to the core diamagnetism and temperature independent paramagnetic contributions such as Pauli paramagnetism), and θ_{CW} is the Curie-Weiss constant. The best fit for both directions was obtained in the temperature range of 150-300 K. θ_{CW} obtained from the fit is \sim -11.1 (2) K when H \perp ab and \sim -17.9 (1) K when H//a; the negative sign suggests antiferromagnetic interaction within the fitted temperature range. The effective moment (μ_{eff}) per Dy is calculated by μ_{eff} /Dy = $\sqrt{8C}$ /3 μ_B , which leads to 6.98 (1) μ_B /Dy when H \perp ab and 5.74 (1) μ_B /Dy when H//a, both of which are far below the expected value of Dy²⁺ (10.6 μ_B), Dy³⁺ (10.65 μ_B)

and Dy⁴⁺ (9.72 μ_B). The small μ_{eff} may be due to the intermediate *f*-electron configuration of Dy in our material.³⁸ The difference between μ_{eff} from two directions may originate from the strong magnetic anisotropy.

To further understand the magnetic behaviors of Dy_{3.00(1)}Pt₂Sb_{4.48(2)}, the hysteresis loops were measured as shown in Figure 4(b) and 4(d). For $H \perp ab$, several metamagnetic transitions can be seen in Figure 4(b). To better visualize it, a plot from 0 to 7 T for the first cycle of the loop and its first derivative is placed on the bottom-right corner of Figure 4(b). Four obvious peaks at $H_{M1} \sim 0.25$ T, $H_{M2} \sim 1.1$ T, $H_{M3} \sim 3.5$ T and $H_{M4} \sim 5.1$ T can be found in the derivative curve under 2K, which correspond to four metamagnetic transitions. The other inset on the top-left corner is the enlarged region between -1.5 T and 1.5 T for the loop. No remanent magnetization can be found, and it indicates that there is no significant ferromagnetic component in Dy_{3.00(1)}Pt₂Sb_{4.48(2)}, i.e., spins are not canted. Under 2 K, the magnetization at 7 T is \sim 7.7 μ B/Dy. When the temperature is raised up to 30 K, a nearly linear relation can be observed. Similarly, the measurement of the hysteresis loop on the other field direction (H//a) was also performed. Not surprisingly, strong magnetic anisotropy leads to completely different features for H/a. No obvious metamagnetic transition can be seen in Figure 4(d), instead, two slop changes for the hysteresis loop measured under 2 K are observed, evidenced by the magenta dM/dH curve in the inset. The hysteresis loop does not show any trend to saturate when H//a at 2 K. Electrical Transport Measurements: Figures 5(a) and 5(b) illustrate the temperature-dependent resistivity and magnetoresistance of Dy_{3,00(1)}Pt₂Sb_{4,48(2)}. When no magnetic field is applied, the electrical resistivity of the material decreases with decreasing temperature, indicating the metallic nature, which is further supported by the electronic structure shown in Figure S2. A kink is found ~ 15.5 K in the main panel of Figure 5(a), which reflects the magnetic transition observed at T_{N1} in Figure 4(a) and 4(c). When plotting the first derivative of the ρ vs T curve, two features at ~5 K ad ~9 K can be found. The 5-K transition corresponds with the magnetic transition at T_{N2} while the 9-K transition might originate from another magnetic transition that was not clearly observed in our magnetic measurement. When the magnetic field is applied perpendicularly to the ab plane, two peaks, one at ~3.5 T and one at ~5.1 T, can be observed for the magnetoresistance curve at 2.5 K in Figure 5(b). The two peaks are consistent with the two metamagnetic transitions seen in Figure 4(b) at H_{M3} and H_{M4}. Although more features are observed under lower field in the magnetic hysteresis loop for

 $H \perp ab$, no obvious transitions can be found in the magnetoresistance measurements. This is primarily due to the intrinsically low resistivity of the sample and, thus, the low-field metamagnetic transitions are possibly obscured by the noise. Interestingly, when the system is warmed up to 6 K, which is above the T_{N1} , the peaks at H_{M3} and H_{M4} disappear while a broad peak emerges at ~4.5 T which persists until 15 K and disappears at 50 K. The broad peak may originate from another metamagnetic transition corresponding with T_{N1} .

Based on the findings above, a brief discussion about the magnetic properties of Dy_{3.00(1)}Pt₂Sb_{4.48(2)} shall be made here. Two magnetic transitions are found in the temperature-dependent magnetic susceptibility curves for both directions at $T_{N1} \sim 3.8$ K and $T_{N2} \sim 15$ K. However, the higher-temperature one is more predominant when $H \perp ab$ while when H//a, the lower-temperature one prevails. Considering the distinct fitted θ_{CW} , we speculate that there are two AFM sublattices in $Dy_{3.00(1)}Pt_2Sb_{4.48(2)}$ which correspond to T_{N1} and T_{N2} in χ vs T curves, i.e., AFM1 that corresponds with T_{N1} and AFM2 that corresponds with T_{N2}. Complex interactions between the two AFM sublattices may lead to the multiple metamagnetic transitions in the hysteresis loops at 2 K. Supported by the transport measurement, the two major metamagnetic transitions at H_{M3} and H_{M4} are correlated with the AFM2 sublattice. Besides the speculation above, another possibility of the magnetic structure could be that one Dy sublattice is responsible for different interaction and coupling constants along different crystallographic directions. In the meantime, the other Dy sublattice results in different magnetic orderings with decreasing temperature, such as spin-reorientations etc. Based on the complex observation further studies including X-Ray Magnetic Circular Dichroism (XMCD) measurements need to be conducted to better interpret the magnetic structure of Dy_{3.00(1)}Pt₂Sb_{4.48(2)}, especially the relation between the magnetic structure and the two settings of disordered Dy and Sb.

Conclusions

In this paper, motivated by the previously reported material type, Y₃Pt₄Ge₆, with both square net and triangular lattices of rare-earth elements, we synthesized mm-sized single crystals of a new material Dy_{3.00(1)}Pt₂Sb_{4.48(2)}, which crystallizes in a Y₃Pt₄Ge₆-type-related structure. Based on the magnetic properties' measurements, we observed two transitions for AFM ordering at ~15 K and ~4 K, which might originate from two competing AFM sublattices. Furthermore, strong magnetic anisotropy and metamagnetic transitions were found for Dy_{3.00(1)}Pt₂Sb_{4.48(2)}. Therefore, further studies

including XMCD measurements should be carried out to better understand the complex spin structure of this material. An unusual valence state of Dy was also seen extrapolated from the Curie-Weiss fitting for the effective moment, which deserves follow-up investigations. The magnetic complexity and crystallographic disorder of Dy_{3.00(1)}Pt₂Sb_{4.48(2)} along with the availability of single crystals provides a platform for investigating magnetism in such structural motifs when Dy is substituted by other rare-earth elements.

Associated Content

Supporting Information

The Supporting Information is available free of charge at XXX.

Crystallographic data of the title compound under different constraints. The elemental analysis based on EDS. The powder X-ray diffraction pattern. The proposed magnetic phase diagram.

Author Information

Corresponding Author: xig75@pitt.edu

Notes: The authors declare no competing financial interest.

Acknowledgements

T.L.P., C.W. and X.G. are supported by the startup fund from the University of Pittsburgh and the Pitt Momentum Fund. Y.D.G. and Z.Q.M. acknowledge the support by the US Department of Energy under grants DE-SC0019068 and DE-SC0014208 (support for magnetic and transport measurements).

References

- (1) Chamorro, J. R.; McQueen, T. M.; Tran, T. T. Chemistry of Quantum Spin Liquids. *Chem. Rev.* **2021**, *121*, 2898–2934.
- (2) Knolle, J.; Moessner, R. A Field Guide to Spin Liquids. *Annu. Rev. Condens. Matter Phys.* **2019**, *10*, 451–472.
- (3) Wen, J.; Yu, S.-L.; Li, S.; Yu, W.; Li, J.-X. Experimental Identification of Quantum Spin Liquids. *npj Quantum Mater.* **2019**, *4*, 12.
- (4) Paddison, J. A. M.; Daum, M.; Dun, Z.; Ehlers, G.; Liu, Y.; Stone, M. B.; Zhou, H.; Mourigal, M. Continuous Excitations of the Triangular-Lattice Quantum Spin Liquid YbMgGaO₄. *Nat. Phys.* **2017**, *13*, 117–122.
- (5) Shen, Y.; Li, Y. D.; Wo, H.; Li, Y.; Shen, S.; Pan, B.; Wang, Q.; Walker, H. C.; Steffens, P.; Boehm, M.; Hao, Y.; Quintero-Castro, D. L.; Harriger, L. W.; Frontzek, M. D.; Hao, L.; Meng, S.; Zhang, Q.; Chen, G.; Zhao, J. Evidence for a Spinon Fermi Surface in a Triangular-Lattice Quantum-Spin-Liquid Candidate. *Nature* **2016**, *540*, 559–562.

- (6) Li, Y.; Chen, G.; Tong, W.; Pi, L.; Liu, J.; Yang, Z.; Wang, X.; Zhang, Q. Rare-Earth Triangular Lattice Spin Liquid: A Single-Crystal Study of YbMgGaO4. *Phys. Rev. Lett.* **2015**, *115*, 167203.
- (7) Han, T. H.; Helton, J. S.; Chu, S.; Prodi, A.; Singh, D. K.; Mazzoli, C.; Müller, P.; Nocera, D. G.; Lee, Y. S. Synthesis and Characterization of Single Crystals of the Spin- 1/2 Kagome-Lattice Antiferromagnets Zn_xCu_{4-x}(OH)₆Cl₂. *Phys. Rev. B* **2011**, *83*, 100402.
- (8) Fu, M.; Imai, T.; Han, T.-H.; Lee, Y. S. Evidence for a Gapped Spin-Liquid Ground State in a Kagome Heisenberg Antiferromagnet. *Science* **2015**, *350*, 655–658.
- (9) Khuntia, P.; Velazquez, M.; Barthélemy, Q.; Bert, F.; Kermarrec, E.; Legros, A.; Bernu, B.; Messio, L.; Zorko, A.; Mendels, P. Gapless Ground State in the Archetypal Quantum Kagome Antiferromagnet ZnCu₃(OH)₆Cl₂. *Nat. Phys.* **2020**, *16*, 469–474.
- (10) Sibille, R.; Lhotel, E.; Pomjakushin, V.; Baines, C.; Fennell, T.; Kenzelmann, M. Candidate Quantum Spin Liquid in the Ce³⁺ Pyrochlore Stannate Ce₂Sn₂O₇. *Phys. Rev. Lett.* **2015**, *115*, 097202.
- (11) Powell, M.; Sanjeewa, L. D.; McMillen, C. D.; Ross, K. A.; Sarkis, C. L.; Kolis, J. W. Hydrothermal Crystal Growth of Rare Earth Tin Cubic Pyrochlores, RE₂Sn₂O₇ (RE = La-Lu): Site Ordered, Low Defect Single Crystals. *Cryst. Growth Des.* **2019**, *19*, 4920–4926.
- (12) Sibille, R.; Gauthier, N.; Lhotel, E.; Porée, V.; Pomjakushin, V.; Ewings, R. A.; Perring, T. G.; Ollivier, J.; Wildes, A.; Ritter, C.; Hansen, T. C.; Keen, D. A.; Nilsen, G. J.; Keller, L.; Petit, S.; Fennell, T. A Quantum Liquid of Magnetic Octupoles on the Pyrochlore Lattice. *Nat. Phys.* **2020**, *16*, 546–552.
- (13) Dissanayake, S.; Shi, Z.; Rau, J. G.; Bag, R.; Steinhardt, W.; Butch, N. P.; Frontzek, M.; Podlesnyak, A.; Graf, D.; Marjerrison, C.; Liu, J.; Gingras, M. J. P.; Haravifard, S. Towards Understanding the Magnetic Properties of the Breathing Pyrochlore Compound Ba₃Yb₂Zn₅O₁₁ through Single-Crystal Studies. *npj Quantum Mater.* **2022**, *7*, 1–11.
- (14) Bag, R.; Dissanayake, S. E.; Yan, H.; Shi, Z.; Graf, D.; Choi, E. S.; Marjerrison, C.; Lang, F.; Lancaster, T.; Qiu, Y.; Chen, W.; Blundell, S. J.; Nevidomskyy, A. H.; Haravifard, S. Beyond Single Tetrahedron Physics of the Breathing Pyrochlore Compound Ba₃Yb₂Zn₅O₁₁. *Phys. Rev. B* **2023**, *107*, L140408.
- (15) Anderson, P. W. The Resonating Valence Bond State in La₂CuO₄ and Superconductivity. *Science* **1987**, *235*, 1196–1198.
- (16) Mustonen, O.; Vasala, S.; Sadrollahi, E.; Schmidt, K. P.; Baines, C.; Walker, H. C.; Terasaki, I.; Litterst, F. J.; Baggio-Saitovitch, E.; Karppinen, M. Spin-Liquid-like State in a Spin-1/2 Square-Lattice Antiferromagnet Perovskite Induced by D¹⁰–D⁰ Cation Mixing. *Nat. Commun.* 2018, 9, 1085.
- (17) Yamaguchi, H.; Uemoto, N.; Okubo, T.; Kono, Y.; Kittaka, S.; Sakakibara, T.; Yajima, T.; Shimono, S.; Iwasaki, Y.; Hosokoshi, Y. Gapped Ground State in a Spin-1/2 Frustrated Square Lattice. *Phys. Rev. B* **2021**, *104*, L060411.
- (18) Godoy, P. F.; Schmidt, M.; Zimmer, F. M. The Ising Model on the Layered J₁-J₂ Square Lattice. *Phys. Lett. A* **2020**, *384*, 126687.
- (19) Venturini, G.; Malaman, B. Crystal Structure of Y₃Pt₄Ge₆: An Intergrowth of BaAl₄ and YIrGe₂ Slabs. *J. Less-Common Met.* **1990**, *167*, 45–52.
- (20) Eustermann, F.; Eilers-Rethwisch, M.; Renner, K.; Hoffmann, R. D.; Pöttgen, R.; Janka, O. Magnetic Properties of the Germanides RE₃Pt₄Ge₆ (RE = Y, Pr, Nd, Sm, Gd-Dy). *Z. Naturforsch. B* **2017**, *72*, 855–864.

- (21) Janka, O.; Hoffmann, R. D.; Eilers-Rethwisch, M.; Rodewald, U. C.; Niehaus, O.; Pöttgen, R. Revisiting Ce₃Pt₄Ge₆-Crystal Structure and Physical Properties. *Inorg. Chem. Front.* **2016**, *3*, 1289–1296.
- (22) Gribanov, A.; Rogl, P.; Grytsiv, A.; Seropegin, Y.; Giester, G. Novel Intermetallic Yb \sim 3Pt \sim 4Si_{6-x} (x = 0.3) A Disordered Variant of the Y₃Pt₄Ge₆-Type. *J. Alloys Compd.* **2013**, *571*, 93–97.
- (23) Sheldrick, G. M. Crystal Structure Refinement with SHELXL. Acta Cryst. C 2015, 71, 3-8.
- (24) Walker, N.; Stuart, D. An Empirical Method for Correcting Diffractometer Data for Absorption Effects. *Acta Cryst. A* **1983**, *39*, 158–166.
- (25) Elstner, M.; Porezag, D.; Jungnickel, G.; Elsner, J.; Haugk, M.; Frauenheim, Th.; Suhai, S.; Seifert, G. Self-Consistent-Charge Density-Functional Tight-Binding Method for Simulations of Complex Materials Properties. *Phys. Rev. B* **1998**, *58*, 7260–7268.
- (26) Andersen, O. K.; Jepsen, O. Explicit, First-Principles Tight-Binding Theory. *Phys. Rev. Lett.* **1984**, *53*, 2571.
- (27) Krier, G., Jepsen, O.; Burkhardt, A.; Andersen, O.K. The TB-LMTO-ASA program. *Stuttgart*, **1995**, *April*.
- (28) Dronskowski, R.; Blöchl, P. E. Crystal Orbital Hamilton Populations (COHP). Energy-Resolved Visualization of Chemical Bonding in Solids Based on Density-Functional Calculations. *J. Phys. Chem.* **1993**, *97*, 8617–8624.
- (29) Wimmer, E.; Krakauer, H.; Weinert, M.; Freeman, A. J. Full-Potential Self-Consistent Linearized-Augmented-Plane-Wave Method for Calculating the Electronic Structure of Molecules and Surfaces: O₂ Molecule. *Phys. Rev. B* **1981**, *24*, 864–875.
- (30) Schwarz, K.; Blaha, P. Solid State Calculations Using WIEN2k. *Comput. Mater. Sci.* **2003**, *28*, 259–273.
- (31) Perdew, J. P.; Wang, Y. Accurate and Simple Analytic Representation of the Electron-Gas Correlation Energy. *Phys. Rev. B* **1992**, *45*, 13244–13249.
- (32) King-Smith, R. D.; Vanderbilt, D. Theory of Polarization of Crystalline Solids. *Phys. Rev. B* **1993**, *47*, 1651–1654.
- (33) Brixner, L. H. Structure and Electrical Properties of Some New Rare Earth Arsenides, Antimonides and Tellurides. *J. Inorg. Nucl. Chem.* **1960**, *15*, 199–201.
- (34) Holbourn, P.E. and Woodhams, F.W.D. A ¹²¹Sb Mössbauer Investigation of the Rare Earth Antimonides. *J. Solid State Chem.* **1981**, *39*, 186-194.
- (35) Barrett, C.S.; Cucka, P.; Haefner, K.J.A.C. The Crystal Structure of Antimony at 4.2, 78 and 298 K. *Acta Cryst.* **1963**, *16*, 451-453.
- (36) Ban, Z.; Sikirica, M. The Crystal Structure of Ternary Silicides ThM₂Si₂(M = Cr, Mn, Fe, Co, Ni and Cu). *Acta Cryst.* **1965**, *18*, 594–599.
- (37) Szytuła, A.; Penc, B.; Hofmann, M.; Przewoźnik, J. Antiferromagnetism of ThCr₂Si₂. *Solid State Commun.* **2012**, *152*, 1027–1029.
- (38) Debray, D.; Wortmann, B.F.; Methfessel, S. Bulk Magnetic Behaviour and Metamagnetism of Some Rare Earth–Zinc (RZn₂; R=Eu, Dy, Er, and Tm) Intermetallics. *Phys. Status Solidi A* **1975**, 30, 713-720.
- (39) *International Tables for Crystallography: Physical Properties of Crystals*, 2nd ed.; Authier, A., Ed.; John Wiley and Sons, 2013; Vol. D.

Table 1. Single crystal structure refinement for Dy_{3.00(1)}Pt₂Sb_{4.48(2)} at 273 (2) K.

	3 ()
Refined Formula	$Dy_{3.00(1)}Pt_2Sb_{4.48(2)}$
F.W. (g/mol)	1423.14
Space group; Z	$P 2_1/m; 2$
a (Å)	8.6252 (8)
b (Å)	4.3109 (3)
c (Å)	12.968 (1)
β(°)	99.609 (3)
$V(Å^3)$	475.43 (7)
Extinction Coefficient	0.00037 (5)
θ range (°)	3.090-31.902
No. reflections; R_{int}	23877; 0.0329
No. independent reflections	1699
No. parameters	75
R_1 : ωR_2 ($I > 2\delta(I)$)	0.0272; 0.0432
Goodness of fit	1.151
Diffraction peak and hole (e ⁻ / Å ²	3) 2.954; -2.613

Table 2. Atomic coordinates and equivalent isotropic displacement parameters for $Dy_{3.00(1)}Pt_2Sb_{4.48(2)}$ at 273 (2) K. (U_{eq} is defined as one-third of the trace of the orthogonalized U_{ij} tensor (\mathring{A}^2))

Atom	Wyck.	Occ.	x	y	z	U_{eq}
Pt1	2e	1	0.52636 (4)	1/4	0.61894 (3)	0.0044 (1)
Pt2	2e	1	0.03314 (4)	1/4	0.61904(3)	0.0045 (1)
Dy1	2e	0.830(1)	0.23486 (7)	1/4	0.43955 (5)	0.0042 (1)
Sb1	2e	0.200(3)	0.4155 (4)	3/4	0.5623 (3)	0.0051 (7)
Sb1'	2e	0.201(3)	0.1156 (4)	3/4	0.5621 (3)	0.0051 (7)
Dy2	2e	0.170(1)	0.2648 (3)	3/4	0.5606(2)	0.0042(1)
Sb2	2e	0.039(2)	0.384(2)	1/4	0.439(1)	0.0051 (7)
Sb2'	2e	0.039(2)	0.083(2)	1/4	0.437 (1)	0.0051 (7)
Dy3	2e	1	0.57655 (6)	3/4	0.81070 (4)	0.0050(1)
Dy4	2e	1	0.07890(6)	3/4	0.81115 (4)	0.0050(1)
Sb3	2e	1	0.12475 (7)	1/4	0.99840 (5)	0.0053 (1)
Sb4	2e	1	0.37569 (7)	3/4	0.00186 (5)	0.0054(1)
Sb5	2 <i>e</i>	1	0.31256 (7)	1/4	0.74994 (5)	0.0051(1)
Sb6	2e	1	0.81150 (7)	1/4	0.74621 (5)	0.0049(1)

Table 3. Anisotropic thermal displacement parameters for Dy_{3.00(1)}Pt₂Sb_{4.48(2)}.

Atom	U11	U22	U33	U23*	U13*	U12*
Pt1	0.0050(2)	0.0040(2)	0.0049(2)	0	0.0009(1)	0
Pt2	0.0049 (2)	0.0042(2)	0.0049(2)	0	0.0009(1)	0
Dy1	0.0020(2)	0.0030(2)	0.0048 (2)	0	0.0013 (2)	0
Sb1	0.003(2)	0.004(2)	0.008(2)	0	0.0003 (10)	0
Sb1'	0.005(2)	0.005(2)	0.008(2)	0	0.002(1)	0
Dy2	0.019(1)	0.011(1)	0.009(1)	0	-0.0003 (9)	0
Sb2	0.021 (9)	0.019 (9)	0.016(8)	0	0.006(6)	0
Sb2'	0.016(8)	0.012(8)	0.008(8)	0	0.001 (5)	0
Dy3	0.0057 (2)	0.0045 (2)	0.0053(2)	0	0.0011(1)	0
Dy4	0.0056(2)	0.0043 (2)	0.0054(2)	0	0.0010(1)	0
Sb3	0.0061 (3)	0.0050(3)	0.0056(3)	0	0.0012 (2)	0
Sb4	0.0057(3)	0.0053 (3)	0.0057(3)	0	0.0012(2)	0
Sb5	0.0043 (3)	0.0048 (3)	0.0067(3)	0	0.0013 (2)	0
Sb6	0.0043 (3)	0.0045 (3)	0.0064(3)	0	0.0013 (2)	0

^{*}For an explanation of the anisotropic thermal displacement parameters, see *The International Tables for Crystallography*³⁹, A. Authier editor, second edition, volume D, pages 231 to 245, John Wiley and Sons, 2014.

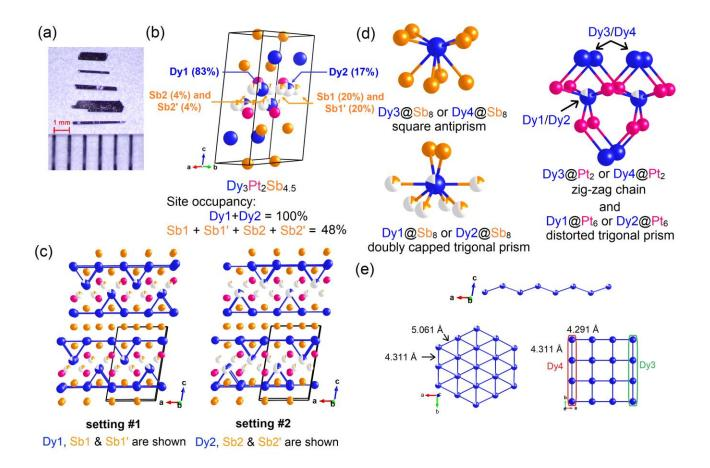


Figure 1. (a) Pictures of the Dy_{3.00(1)}Pt₂Sb_{4.48(2)} crystals under an optical microscope. The composition is from single-crystal X-ray diffraction results. **(b)** Unit cell and structure of Dy_{3.00(1)}Pt₂Sb_{4.48(2)} with all disordered sites where blue, red, and orange spheres represent Dy, Pt and Sb atoms, respectively. **(c)** The two different settings of Dy_{3.00(1)}Pt₂Sb_{4.48(2)} with distinct disordered sites of Dy and Sb. **(d)** The coordination environment of Dy represented by setting#1. **(e)** Dy-Dy frameworks represented by setting#1.

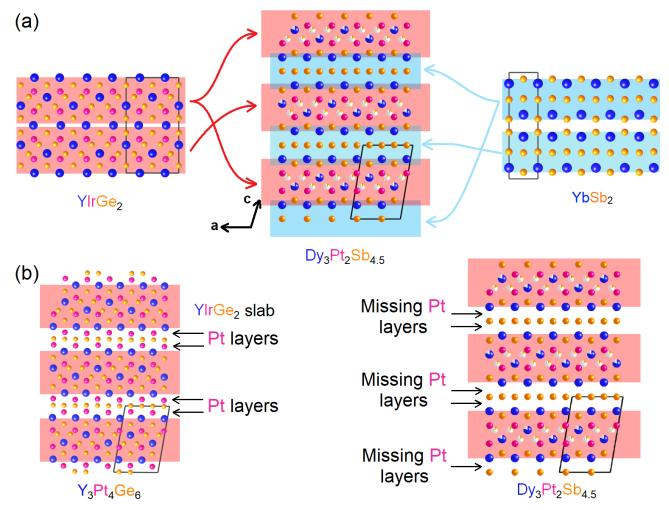


Figure 2. (a) The relation among structural motifs of YIrGe₂ (left), Dy₃Pt₂Sb_{4.48} (middle) and YbSb₂ (right). The shaded parts with the same color are similar to each other and the arrows indicate the location of the intergrowth. **(b)** Comparison between the structures of Y₃Pt₄Ge₆ and Dy₃Pt₂Sb_{4.48}. The red shades stand for the common YIrGe₂ slabs in both structural types. The arrows indicate where the absences of Pt atoms happen.

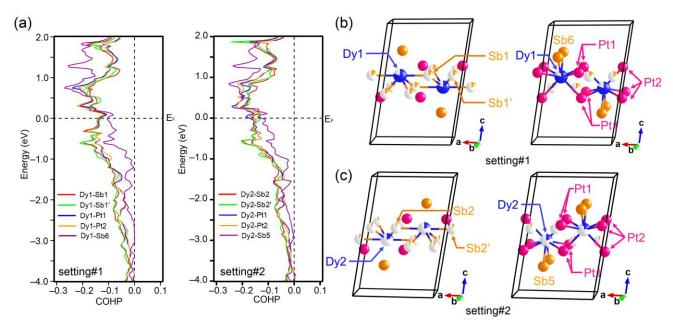


Figure 3. (a) The COHP curves for both settings of Dy₃Pt₂Sb_{4.48}. (b) & (c) Visualization of related chemical bonds mentioned in (a).

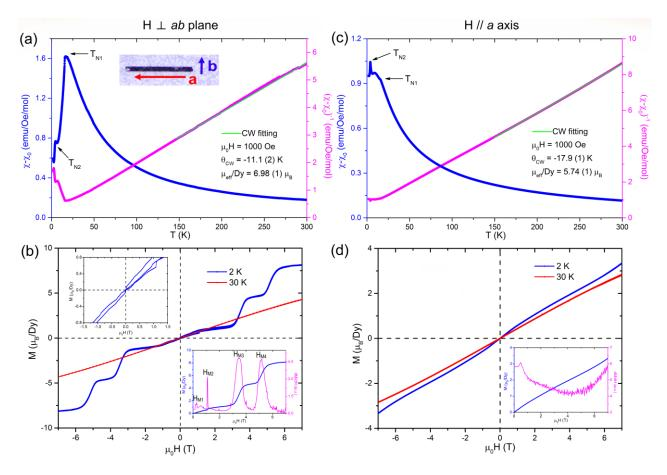


Figure 4. The temperature dependence of magnetic susceptibility and inverse magnetic susceptibility when the external magnetic field is (a) perpendicular to the ab plane; (c) parallel to the a axis. The inset of (a) is a picture of crystal shown the direction of crystallographic axes. (Main panel) The hysteresis loop of $Dy_3Pt_2Sb_{4.48}$ under various temperatures when the external magnetic field is (b) perpendicular to the ab plane; (d) parallel to the a axis. The inset figures in (b) are (top left) enlarged hysteresis loop at 2 K from -1.5 T to 1.5 T and (bottom right) M vs H curve from 0 to 7 T with its first derivative. The inset in (d) is the M vs H curve from 0 to 7 T with its first derivative.

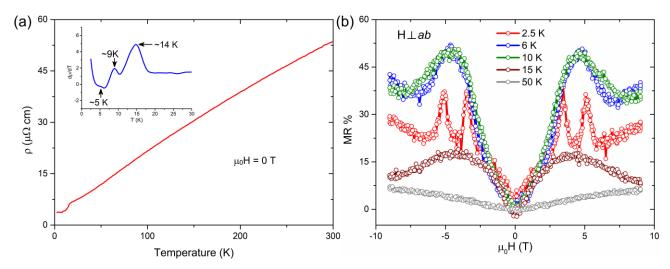


Figure 5. (a) (Main panel) Temperature-dependent electrical resistivity with no magnetic field applied. **(Inset)** The first derivative of the main panel figure. **(b)** Magnetoresistance measured from -9 T to 9 T at various temperatures when the magnetic field is applied perpendicularly to the ab plane.

Supplementary Information

Crystallographic Disorder and Strong Magnetic Anisotropy in Dy₃Pt₂Sb_{4.48}

Terry Paske,^a Yingdong Guan,^b Chaoguo Wang,^a Curtis Moore,^c Zhiqiang Mao,^b Xin Gui ^{a*}

Table of Contents

Table S1	S2
Table S2	S3
Figure S1	S4
Figure S2	S5
Figure S3	S6

^a Department of Chemistry, University of Pittsburgh, Pittsburgh, PA, 15260, USA

^b Department of Physics, Pennsylvania State University, University Park, PA, 16801, USA

^c Department of Chemistry and Biochemistry, The Ohio State University, Columbus, OH, 43210, USA

Table S1. Comparsison of single crystal structure refinement results for $Dy_{3.00(1)}Pt_2Sb_{4.50(2)}$ at 273 (2) K.

Refined Formula	Dy3.00(1)Pt2Sb4.50(2)	No Sb2 and Sb2'	No Sb2/2' and Dy2
F.W. (g/mol)	1424.95	1424.95	1424.95
Space group; Z	$P 2_1/m; 2$	$P 2_1/m; 2$	$P 2_1/m; 2$
a (Å)	8.6252 (8)	8.6252 (8)	8.6252 (8)
b (Å)	4.3109 (3)	4.3109 (3)	4.3109 (3)
c (Å)	12.968 (1)	12.968 (1)	12.968 (1)
β (°)	99.609 (3)	99.609 (3)	99.609 (3)
V (Å ³)	475.43 (7)	475.43 (7)	475.43 (7)
Extinction Coefficient	0.00040 (4)	0.00032 (5)	0.00000 (13)
θ range (°)	3.090-31.902	3.090-31.902	3.090-31.902
No. reflections; R_{int}	23877; 0.0329	23877; 0.0329	23877; 0.0329
No. independent reflections	1699	1699	1699
No. parameters	91	79	71
R_1 : ωR_2 (I >2 $\delta(I)$)	0.0257; 0.0392	0.0316; 0.0500	0.0845; 0.1405
Goodness of fit	1.143	1.431	3.971
Diffraction peak and hole (e ⁻ / Å ³)	2.098; -2.257	8.992; -2.445	58.807; -5.725

Table S2. The atomic ratios from Energy-Dispersive X-ray Spectroscopy (EDS) result of two different crystals of Dy₃Pt₂Sb_{4.5}.

	Dy% (Error%)	Pt% (Error%)	Sb% (Error%)
Number of points		Sample1	
1	34.71 (3.95)	22.71 (7.93)	42.58 (4.72)
2	34.74 (3.88)	22.15 (7.99)	43.11 (4.66)
3	34.68 (3.83)	22.02 (7.28)	43.31 (4.65)
4	34.89 (3.91)	22.30 (7.54)	42.81 (4.84)
5	34.77 (3.92)	22.45 (8.10)	42.78 (4.84)
Number of points		Sample2	
1	34.81 (3.93)	22.99 (7.75)	42.20 (4.90)
2	34.86 (3.88)	22.80 (7.38)	42.35 (4.88)
3	34.75 (3.85)	22.87 (8.03)	42.38 (4.87)
4	35.06 (3.94)	22.63 (7.79)	42.31 (4.86)
5	34.99 (3.94)	22.51 (7.86)	42.50 (4.84)
Average	34.82 (3.90)	22.54 (7.77)	42.63 (4.81)
Normalized to Pt	3.1 (3)	2.0 (7)	3.8 (4)

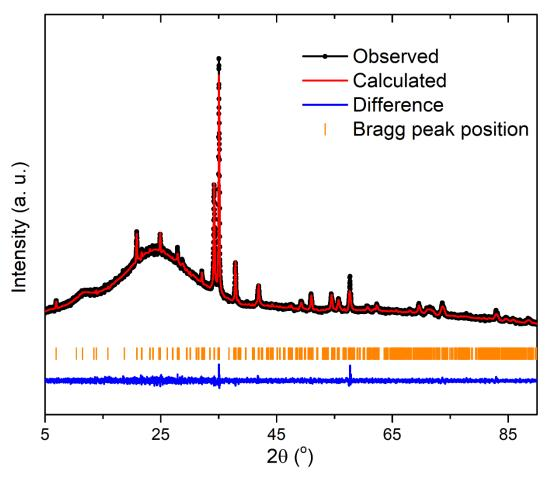


Figure S1. Powder XRD pattern of the crushed crystals of Dy_{3.00(1)}Pt₂Sb_{4.48(2)}. Blue and red lines stand for calculated and observed patterns, respectively. The crushed crystals show a preferred orientation of (001) so that the observed peak for, for instance, (005) peak is much higher than calculated. Therefore, a refinement for preferred orientation of (001) has been conducted.

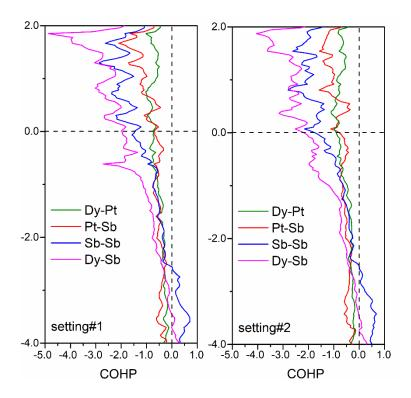


Figure S2. COHP curves of Dy_{3.00(1)}Pt₂Sb_{4.48(2)} for both settings.

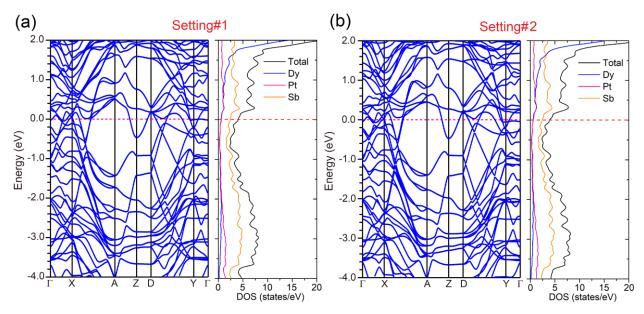


Figure S3. Band structure and DOS of $Dy_{3.1(3)}Pt_{2.0(7)}Sb_{3.8(4)}$ for (a) setting#1 and (b) setting#2.